Impact of rainfall extremes on energy exchange and surface temperature anomalies across biomes in the Horn of Africa

Temesgen Alemayehu Abera[a,b,*], Janne Heiskanen[a,b], Petri K.E. Pellikka[a,b], Eduardo Eiji Maeda[a]

[a] Department of Geosciences and Geography, P.O. Box 68, FI-00014 University of Helsinki, Finland
[b] Institute for Atmospheric and Earth System Research, Faculty of Science, University of Helsinki, Finland

ABSTRACT

Precipitation extremes have a strong influence on the exchange of energy and water between the land surface and the atmosphere. Although the Horn of Africa has faced recurrent drought and flood events in recent decades, it is still unclear how these events impact energy exchange and surface temperature across different ecosystems. Here, we analyzed the impact of precipitation extremes on spectral albedo (total shortwave, visible, and near-infrared (NIR) broadband albedos), energy balance, and surface temperature in four natural vegetation types: forest, savanna, grassland, and shrubland. We used remotely sensed observations of surface biophysical properties and climate from 2001 to 2016. Our results showed that, in forests and savannas, precipitation extremes led to divergent spectral changes in visible and NIR albedos, which cancelled each other limiting shortwave albedo changes. An exception to this pattern was observed in shrublands and grasslands, where both visible and NIR albedo increased during drought events. Given that shrublands and grasslands occupy a large fraction of the Horn of Africa (52%), our results unveil the importance of these ecosystems in driving the magnitude of shortwave radiative forcing in the region. The average regional shortwave radiative forcing during drought events (-0.64 W m^{-2}, SD 0.11) was around twice that of the extreme wet events (0.33 W m^{-2}, SD 0.09). Such shortwave forcing, however, was too small to influence the surface–atmosphere coupling. In contrast, the surface feedback through turbulent flux changes was strong across vegetation types and had a significant ($P < 0.05$) impact on the surface temperature and net radiation anomalies, except in forests. The strongest energy exchange and surface temperature anomalies were observed over grassland and the smallest over forest, which was shown to be resilient to precipitation extremes. These results suggest that land management activities that support forest preservation, afforestation, and reforestation can help to mitigate the impact of drought through their role in modulating energy fluxes and surface temperature anomalies in the region.

1. Introduction

Precipitation extremes across the Horn of Africa have become more frequent and intense in recent decades (Masih et al., 2014; Lyon and DeWitt, 2012). During 2011, for example, the region faced the worst drought in 60 years (UNDP, 2011). Precipitation volumes during the main rainfall season (March through June) have also declined continuously in recent decades (Nicholson, 2017; Lyon and DeWitt, 2012). Understanding how the ecosystem responded to rainfall variability in the past is a critical step in the prediction of ecosystem response to future extreme events, as well as to set effective adaptation and mitigation strategies.

Precipitation extremes can affect the feedback between the land surface and the atmosphere through different mechanisms. For

instance, extreme events affect soil moisture and vegetation, causing changes in the surface albedo and, consequently, the amount of available energy at the land surface. Drought-induced albedo changes have been studied since the 1970s (Charney et al., 1975). Earlier studies have hypothesized that an albedo increase triggers atmospheric subsidence, weakens convective activity, and leads to less precipitation, further amplifying droughts (Charney et al., 1975).

Although modeling experiments have supported this hypothesis (e.g., Evans et al., 2017; Meng et al., 2014a, 2014b), observation-based studies in Europe have found contradicting evidence (e.g., Teuling and Seneviratne, 2008), arguing that drought-induced albedo changes are too small to have an impact on the surface–atmosphere coupling. The main causes for the small changes in albedo were shown to result from opposite changes in visible (VIS, 0.3–0.7 μm) and near-infrared (NIR,

0.7–5.0 µm) broadband albedos, which canceled each other, limiting changes in the total shortwave (SW) broadband albedo (0.3–5.0 µm) (Teuling and Seneviratne, 2008; Sütterlin et al., 2016). However, it is still unknown if this contrasting albedo pattern exists in shrublands and grasslands, which are the dominant ecosystem in East Africa. Furthermore, previous studies were largely focused on single or few drought events from relatively shorter time series (Teuling and Seneviratne, 2008; Meng et al., 2014a, 2014b). The assessment of multiple extreme events, using longer time series, is needed to understand and ascertain the relationship between climate and albedo variability, as well as the dependence of this relationship on geographic location, seasons, and biomes.

Precipitation extremes are also likely to have an impact on the energy budget and land surface temperature (LST) through their effect on net radiation and turbulent fluxes. This process can change the stability of the planetary boundary layer, playing an important role in the link between land surface and atmosphere (Eltahir, 1998; Betts and Ball, 1998). Their impact can be strong in a water-limited environment compared with a humid environment (Small and Kurc, 2003). This is due to the stronger impact of precipitation extremes in determining the amount of water available for evaporation and transpiration, which directly affects surface temperature (Yin et al., 2014; Betts and Ball, 1998).

Changes in the energy exchange between the land and atmosphere during extreme rainfall events, as well as the resulting surface temperature, vary among vegetation types given that plants respond differently to soil-moisture variability. For instance, during the 2003 European drought, grassland showed stronger energy exchange and LST anomalies in comparison with forests (Teuling et al., 2010). Studies in Mexico also showed strong fluctuation in surface temperature in shrubland and grassland when the driest and wettest periods were compared (Small and Kurc, 2003). Globally, observational evidence to understand and quantify ecosystem-specific responses to climate extremes is still lacking (Miralles et al., 2018). As a result, climate models are still immature in representing the influence of surface feedback on temperature changes (Miralles et al., 2018).

The consequences of this bottleneck are particularly evident in the Horn of Africa, where fragile socioeconomic conditions often make the region susceptible to climate variability. Despite the frequent occurrence of precipitation extremes, it is still unclear how these events impact the energy exchange and surface temperature across major East African ecosystems, such as shrubland, grassland, and savanna. For instance, the impact of precipitation extremes on individual spectral changes in VIS and NIR, which were shown to be critical in driving SW albedo changes in Europe, has not yet been investigated in dominantly arid ecosystems. As a result, the contribution of radiative forcing to surface warming or cooling is still largely unknown.

The objective of this study was to analyze the impact of precipitation extremes on albedo, energy exchange, and surface temperature anomalies in the Horn of Africa during 2001–2016. More specifically, we investigated the impact of rainfall extremes across different ecosystems and seasons on: (1) VIS, NIR, and SW albedo anomalies and the associated radiative forcing, and whether these have any impact on the surface–atmosphere coupling in the region, and (2) anomalies of turbulent fluxes (sensible and latent heat), radiation energy exchanges, and LST.

2. Material and methods

2.1. Study domain

The study area encompasses Kenya, Somalia, Ethiopia, Eritrea, and Djibouti. It represents a large geographic area ($\sim 2.48 \times 10^6$ km^2) in the Horn of Africa and covers a wide range of climate, topography, and vegetation (Fig. 1a–c). The region has a multimodal rainfall pattern and receives up to three rainfall maxima. Eritrea and northern parts of

Ethiopia receive maximum rainfall during June to August. The rest of the region receives "long rains" (the main rainfall season) from March to May (MAM, hereafter) and "short rains" from October to December (OND, hereafter). Such rainfall patterns largely result from the biannual equatorial passage of the Intertropical Convergence Zone and show considerable interannual and intraseasonal variability under the influence of the Indian Ocean dipole, the El Niño–Southern Oscillation, and the Madden–Julian oscillation (Nicholson, 2017; Indeje et al., 2000). In recent decades, precipitation extremes have become very common and severe droughts and floods have prevailed in the region (Li et al., 2016; Masih et al., 2014; Fig. 1d and e). Locally, rainfall patterns are influenced by topography, which ranges from −125 m below sea level in the Danakil Depression in Ethiopia to 5199 m above sea level at the top of Mount Kenya. According to 2001–2016 Tropical Rainfall Measuring Mission (TRMM) data, the mean annual precipitation ranges from 81 to 2130 mm year^{-1} (Fig. 1f).

Based on the Moderate Resolution Imaging Spectroradiometer (MODIS) land cover product (MCD12Q1, collection 6, 500 m resolution; Friedl and Sulla-Menashe, 2015) and the International Geosphere-Biosphere Programme (IGBP) classification scheme, mainly shrubland (open and closed), grassland, savanna (wooded savanna and savanna), bare land, mixed (crop/vegetation), cropland, and forest (mainly evergreen broad-leaf forest) cover the study area. Of these, shrubland covers the largest part (33%), followed by grassland (19%), savanna and bare land (each 16%), mixed crop/vegetation (8%), cropland (5%), forest (2%), and others (1%). Photos of some of the natural vegetation covers are shown in Fig. 2.

2.2. Remote sensing and climate data

To assess the intensity of precipitation extremes during drought and extreme wet events, we used TRMM3B43, version 7, monthly data with a spatial resolution of 0.25°, which are freely available from the Goddard Earth Sciences Data and Information Services Center (GES DISC) (Tropical Rainfall Measuring Mission (TRMM), 2011). This product provides precipitation estimates based on good quality microwave, infrared, and rain gauge data (Huffman et al., 2010) and has been compared with gridded data in Africa and reported to be more feasible for drought monitoring (Naumann et al., 2012). Furthermore, our comparison of TRMM with monthly automatic weather station data in southern Kenya showed moderate agreement (Fig. S1).

For monitoring albedo and LST changes during precipitation extremes, MODIS MCD43C3 Bidirectional Reflectance Distribution Function (BRDF)/Albedo and MOD11A2 LST/Emissivity products were used, respectively. The daily albedo product used here (MCD43C3) has a spatial resolution of 0.05° and was temporally aggregated to a monthly scale to match the other data by taking the average of all daily retrievals in each month. We downloaded this product from the Land Processes Distributed Active Archive Center (LP DAAC) (Schaaf and Wang, 2015). We used VIS (0.3–0.7 µm), NIR (0.7–5.0 µm), and total SW (0.3–5.0 µm) broadband black-sky albedo. We chose black-sky albedo over white-sky albedo given that black-sky albedo represents albedo at local noon and it is consistent in time with the model used in this study for estimating the G/R_n ratio (where G is ground heat flux and R_n is net radiation). Furthermore, the choice of albedo type does not affect our results as they are strongly correlated in the region (Abera et al., 2019).

The LST product (MOD11A2, version 6, 8-day composite), which has a spatial resolution of 1 km, was similarly downloaded from the LP DAAC (Wan et al., 2015). All cloud contaminated pixels were filtered and removed from our analysis using quality control flag bits (i.e., cloud-free and high-quality pixels were identified using quality control flag bits = 0). This product has an accuracy better than 1 K in most cases (Wan et al., 2015).

For inferring the vegetation condition during precipitation extremes, we calculated the enhanced vegetation index (EVI; Huete et al.,
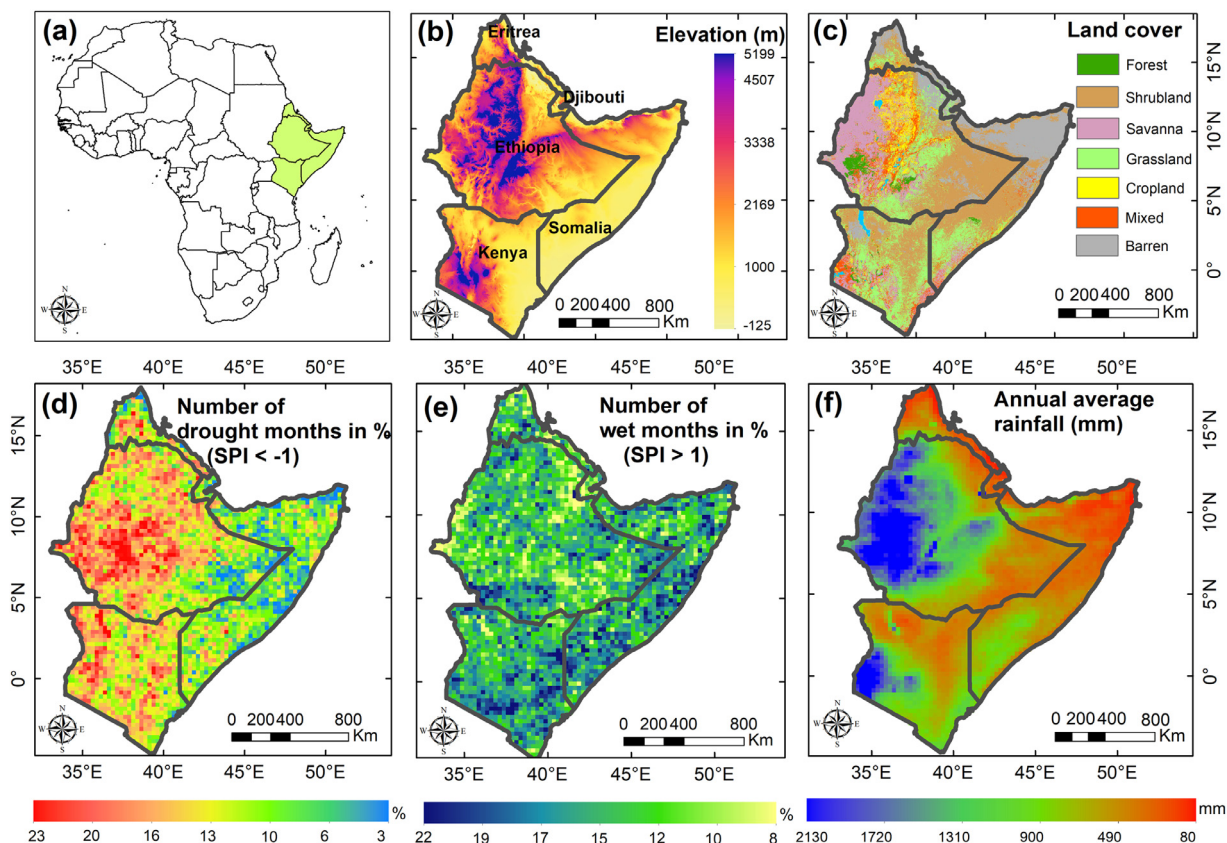
Fig. 1. (a) Location of the study area, (b) topographic elevation (USGS 30 m digital elevation model), (c) MODIS land cover map, (d) number of drought months during 2001–2016, (e) number of extreme wet months during 2001–2016, and (f) annual average rainfall from the Tropical Rainfall Measuring Mission 3B43 data. Drought and extreme wet months represent pixels with a 3-month Standardized Precipitation Index (SPI) of < -1 and >1, respectively. Number expressed in percentage of drought (extreme wet) months from the total number of months in 16 years (192 months).
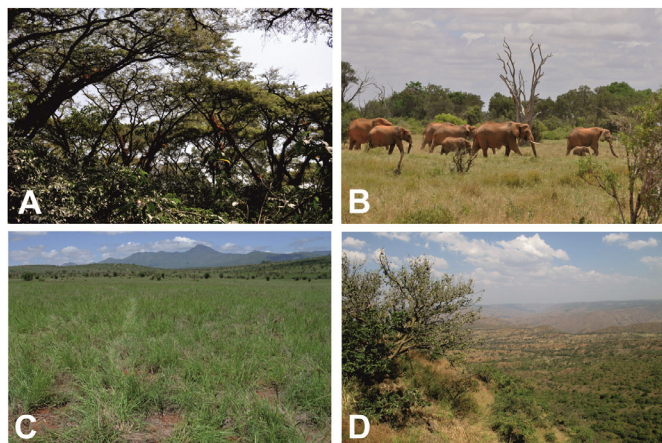

Fig. 2. (A) Forest with tall trees and understory coffee bushes in Kaffa province, southwestern Ethiopia, (B) Savannah with scattered trees and wild animals in Taita Taveta County, southeastern Kenya, (C) Grassland in Taita Taveta County, southeastern Kenya, (D) Shrubland in Central Ethiopia. Photos: Petri Pellikka.

2002):

$$\text{EVI} = 2.5 \times \frac{\rho_{NIR} - \rho_{red}}{\rho_{NIR} + (6 \times \rho_{red} - 7.5 \times \rho_{blue}) + 1} \quad (1)$$

where ρ refers to BRDF corrected reflectance using the BRDF model parameters in red, blue, and NIR bands of the MCD43B1 MODIS product (NASA LP DAAC, 2014). The EVI time series (2001–2016) were corrected for sun-sensor geometry artifacts by fixing the sensor view angle at nadir and sun angle at 45°. EVI, compared with the normalized

difference vegetation index (NDVI), is sensitive to NIR reflectance, less affected by signals from background soil, and has less of a saturation problem over dense canopies (Huete et al., 2002). Furthermore, version 2.0 leaf area index (LAI) data (2001–2016) with 1 km spatial resolution and 10-day temporal resolution were downloaded from the Copernicus Global Land Service (https://land.copernicus.eu/global/products/lai). This product is produced from SPOT VEGETATION and PROBA-V sensors, and 90% of samples meet the Global Climate Observing System accuracy requirements (Verger et al., 2014). In areas with large LAI, it was also reported to have better accuracy than the MODIS LAI (Li et al., 2015).

For the radiation flux anomaly calculation, the 2001–2016 monthly mean downwelling and upwelling SW and longwave (LW) radiation fluxes from the Clouds and the Earth's Radiant Energy System (CERES) Energy Balanced And Filled (EBAF) Surface product (version 4.0, 1° spatial resolution) were used. Radiation fluxes from CERES instruments provide a long-term (2000 to present) global radiation budget, and its measurements were found to be consistent and stable (Dong et al., 2008; Loeb et al., 2009). This product was downloaded from NASA (https://ceres.larc.nasa.gov/products.php?product=EBAF-Surface).

Latent heat flux was retrieved from the Global Land Evaporation Amsterdam Model (GLEAM), version 3.2a, evapotranspiration data (using Eqs. (3) and (4)). This daily product has 0.25° resolution (Martens et al., 2017) and can be downloaded from https://www.gleam.eu/. It uses the Priestley and Taylor evaporation model driven mainly by satellite-observed soil-moisture, vegetation optical depth, air temperature, radiation (e.g., CERES), and precipitation data. Validation of this product showed that it correlates well with eddy-covariance measurements ($r = 0.78$–0.81) (Martens et al., 2017).

Air temperature data, at a monthly timescale and 0.5° × 0.6°

resolution, were downloaded from the Modern-Era Retrospective analysis for Research and Applications (MERRA-2) (https://gmao.gsfc.nasa.gov/reanalysis/MERRA-2/). This product is a screen-level (2 m) air temperature derived from satellite observation and weather data by the Global Modeling and Assimilation Office in the USA. Evaluation of the product against in situ data over land surfaces showed a daily mean and maximum bias of 0.1 K and 1.5 K, respectively (Michael et al., 2015).

Besides, vegetation cover from land cover product (MCD12Q1, version 6, 500 m resolution) (Friedl and Sulla-Menashe, 2015) and the Vegetation Continuous Fields product (MOD44B, version 6, 250 m resolution) for identifying the percentage of soil and vegetation cover in each pixel (Dimiceli et al., 2015) were used.

All data were obtained for the period between 2001 and 2016. The data were temporally and spatially synchronized to a monthly timescale and 0.25° resolution, respectively.

2.3. Identifying the impact of precipitation extremes on albedo

Precipitation extremes were defined based on the 3-month Standardized Precipitation Index (SPI) value using TRMM3B data and refer to drought (SPI ≤ 1) and extreme wet (SPI > 1) events based on World Meteorological Organization (WMO) SPI value classification (WMO, 2012). We chose the MAM ("long rains") and the OND ("short rains") seasons for our analysis as these are the major rainfall seasons in the region. This choice also helps to minimize the impact of periods with little rainfall (or dry periods), where a small deviation in precipitation can give exaggerated (positive or negative) SPI values (WMO, 2012).

To identify the impact of precipitation extremes on VIS, NIR, and SW broadband black-sky albedos, we used the following steps. Long-term trends from the albedo and precipitation data were identified using ordinary least squares regression and were removed from our analysis. This helps to avoid spurious correlations resulting from long-term trends. To investigate albedo change attributed only to climate extremes, pixels affected by land cover conversions, which also cause albedo change (Abera et al., 2019), were discarded from our analysis. For this, stable pixels were identified for the whole region on a pixel-by-pixel basis using the MCD12Q1 time-series data (2001–2016). Then, the frequency of land cover type for each pixel was calculated and pixels with a maximum frequency of 16 were retained (i.e., the maximum frequency for stable pixels during 2001–2016). The remaining 10.8% of pixels (268 324.7 km^2), which have experienced land cover change at least once during the 16-year period, were discarded from our analysis.

We restricted our analysis to the four dominant natural vegetation types in the region (shrubland, grassland, savanna, and forest). This is (1) to reduce the impact of albedo change from other anthropogenic activities, such as land management change through irrigation for agriculture and the application of fertilizers and pesticides (Luyssaert et al., 2014), and (2) due to the difficulty in accurately identifying, for instance, cropland, which often occurs mixed with other vegetation types in the region at 1 km resolution (Zhang et al., 2005; Abera et al., 2018).

Absolute anomalies were calculated using the detrended albedo (VIS, NIR, and SW) data to estimate the albedo change. Then, the average absolute anomalies of albedo were computed for each SPI bin, according to WMO SPI ranges, from the entire time series (2001–2016) for the four land cover types. Furthermore, to check the consistency and robustness of our results over shrubland and grassland, which showed a different NIR pattern during drought in the region, we did the same analysis using an 8-day composite SW black-sky albedo product from the Global LAnd Surface Satellite (GLASS) project with 1 km spatial resolution (Liang and Liu, 2012). GLASS albedo was downloaded from the Global Land Cover Facility (http://glcf.umd.edu/data/abd/). Compared with MODIS (MCD43C3) albedo, GLASS albedo showed similar results during precipitation extremes in the region

(Supplementary Fig. S2).

To statistically explore the impact of precipitation extremes (predictor variable) on albedo (response variable), quantile regression was used. Quantile regression, unlike ordinary least squares regression, does not require any assumption about the underlying data distribution, is robust against outliers in the distribution of the response variable, and estimates the response of a variable in all parts of its data distribution (Koenker, 2005). Meaning, it measures the effects of predictor variable not only in the center of a distribution but also in the lower and upper tails. This helps to understand and investigate the impacts of precipitation extremes on albedo or another environmental variable (e.g., LST) at different intensities (for details of its application on climate extremes refer Gao and Franzke, 2017). Finally, the quantile regression coefficient (y-axis) were plotted for each quantile (10th, 25th, 50th, 75th, and 90th percentile) on the x-axis.

2.4. Estimating the effect of precipitation extremes on the energy balance and land surface temperature anomalies across vegetation types

To quantify the impact of albedo changes on the energy balance during precipitation extremes, average instantaneous SW surface radiative forcing (ISRF) was estimated across vegetation types during 2001–2016:

$$\text{ISRF} = -\text{SW}_{in} * (\Delta\alpha) \tag{2}$$

where SW_{in} is the incoming SW radiation, and $\Delta\alpha$ is the change in SW albedo due to precipitation extreme.

To estimate the impact on radiation and the turbulent energy exchange, first the net radiation (R_n) was calculated from the monthly 2001–2016 CERES EBAF surface flux product for the two seasons (MAM and OND):

$$R_n = (\text{SW}_{in} - \text{SW}_{out}) + (\text{LW}_{in} - \text{LW}_{out}) \tag{3}$$

where SW_{in} is the downwelling SW radiation flux at the surface; SW_{out} is the upwelling SW radiation flux at the surface; LW_{in} is the downwelling LW radiation flux at the surface; and LW_{out} is the upwelling LW radiation flux at the surface. Second, the latent heat flux (ΛE in W m^{-2}) was computed from the GLEAM version 3.2a evapotranspiration data (Dingman, 2015):

$$\Lambda E = \rho_w * \Lambda_v * \text{ET} \tag{4}$$

$$\Lambda_v = 2.495 - (2.36 * 10^{-3}) * (T_{air} - 273) \tag{5}$$

where ρ_w is the density of water (1000 kg m^{-3}); λ_v is the heat of vaporization (MJ kg^{-1}); T_{air} is air temperature (K) from MERRA-2; and ET is evapotranspiration (mm day^{-1}). Third, the G/R_n ratio was estimated using an empirical equation that estimates values near local noon (Bastiaanssen, 2000):

$$\frac{G}{R_n} = (T_s - 273.15)(0.0038 + 0.0074 * \alpha)(1 - 0.98 * \text{NDVI}^4) \tag{6}$$

where G is ground heat flux; T_s is the LST; α is black-sky albedo at local noon and is thus consistent in time with the model; and NDVI is the normalized difference vegetation index (NIR − R/NIR + R, where NIR and R are the near-infrared and red reflectance, respectively, which were corrected from sun-sensor geometry artifacts using the MCD43B1 BRDF/Albedo model parameter). Then, G was obtained by multiplying the G/R_n ratio by the Rn estimated in Eq. (3). Fourth, the sensible heat flux (H) was computed as the closure of the energy balance:

$$H = R_n - (\Lambda E + G) \tag{7}$$

Finally, absolute anomalies were computed for each of the turbulent energy (ΔH and ΛE) as well as radiation energy balance terms (ΔR_n, SW_{in}, SW_{out}, LW_{in}, and LW_{out}) to estimate the change during precipitation extremes, and relationships were explored using quantile regression. Ground heat flux anomalies (ΔG) were very small for all

Mar-Apr-May   Oct-Nov-Dec
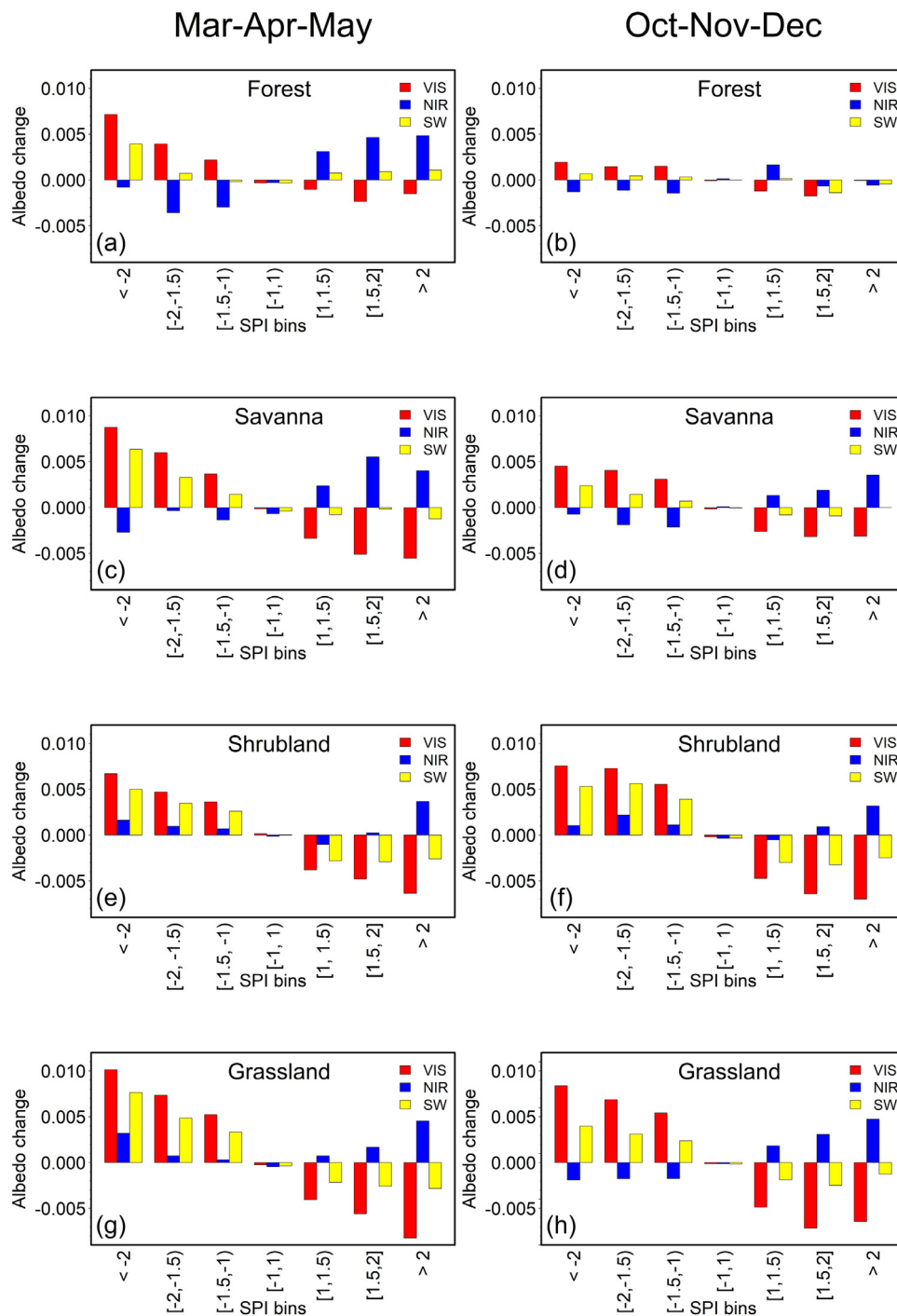
Fig. 3. Average changes in visible (VIS), near-infrared (NIR), and shortwave (SW) broadband albedos for each 3-month Standardized Precipitation Index (SPI) bin during 2001–2016 in the Horn of Africa in forest, savanna, shrubland, and grassland. Left (a, c, e, and g) and right (b, d, f, and h) panels show changes during March–April–May and October–November–December, respectively.

vegetation types in the region and ignored in our analysis (Supplementary Fig. S3).

3. Results

3.1. Albedo changes during precipitation extremes in the Horn of Africa

The average spectral albedo during drought and extreme wet events are displayed in the four vegetation types between 2001 and 2016 (Fig. 3). On average, VIS albedo consistently increased during droughts (SPI ≤ 1) and decreased in extreme wet events (SPI > 1) across all

vegetation types. In NIR, an opposite pattern was observed. The VIS albedo changes during both extreme wet and drought events were stronger in magnitude than the NIR changes, resulting in a net increase in SW albedo during drought in all vegetation types and a decrease in SW albedo during extreme wet events with the exception of forests. Note that the SW broadband albedo product has its own weighting coefficients and anomalies not necessarily equal to the sum of VIS and NIR albedo anomalies (see Liang, 2001 for the coefficients and their calculation).

Forest showed opposite changes in VIS and NIR albedos during both extreme-dry (0.004 vs −0.002) and extreme wet events (−0.002 vs

Table 1

Average spectral changes in albedo (VIS, visible; NIR, near-infrared; SW, shortwave) during drought and extreme wet events in the Horn of Africa (2001–2016). Standard deviation shown in brackets. α, black-sky albedo at local noon; IGBP, International Geosphere-Biosphere Programme; SPI, Standardized Precipitation Index.

IGPB vegetation types	March–April–May/October–November–December					
	Average Δα during drought (SPI < −1)			Average Δα during extreme wet events (SPI > 1)		
	$\Delta\alpha_{VIS}$	$\Delta\alpha_{NIR}$	$\Delta\alpha_{SW}$	$\Delta\alpha_{VIS}$	$\Delta\alpha_{NIR}$	$\Delta\alpha_{SW}$
Forest	0.004 (0.002)/0.002 (0.000)	−0.002 (0.001)/−0.001 (0.000)	0.001 (0.002)/0.000 (0.000)	−0.002 0.001)/−0.001 (0.001)	0.004 (0.001)/0.000 (0.001)	0.001 (0.000)/−0.001 (0.001)
Savanna	0.006 (0.002)/0.004 (0.001)	−0.001 (0.001)/−0.002 (0.001)	0.004 (0.002)/0.002 (0.001)	−0.005 (0.001)/−0.003 (0.000)	0.004 (0.001)/0.002 (0.001)	−0.001 (0.000)/−0.001 (0.000)
Shrubland	0.005 (0.001)/0.007 (0.001)	0.001 (0.000)/0.001 (0.001)	0.004 (0.001)/0.005 (0.001)	−0.005 (0.001)/−0.006 (0.001)	0.001 (0.002)/0.001 (0.002)	−0.003 (0.000)/−0.003(0.000)
Grassland	0.008 (0.002)/0.007 (0.001)	0.001 (0.001)/−0.002 (0.000)	0.005 (0.002)/0.003 (0.001)	−0.006 (0.002)/−0.006 (0.001)	0.002 (0.002)/0.003 (0.001)	−0.003 (0.000)/−0.002 (0.000)

0.004) in MAM, respectively. In extreme wet events, the rise in NIR albedo outweighed the decrease in VIS albedo and hence the SW albedo anomaly increased (0.001). During OND, the changes in albedo were in general minor (Fig. 3a and b and Table 1).

VIS and NIR albedo in savanna showed a consistent and opposite spectral change during drought and extreme wet events in both seasons. However, in MAM droughts, the contrasting spectral changes had a relatively small impact on SW albedo anomalies (0.004) due to the strong VIS albedo increase (0.006), which offset the smaller NIR decrease (−0.001) (Fig. 3c,d and Table 1).

Shrubland, unlike other land cover types, showed an increase in albedo in all spectral ranges during drought events in both seasons (Fig. 3e and f). Such a pattern in shrubland was illustrated in the NIR and VIS albedo anomaly time series (2001–2016), making it the least divergent compared with the others (Table 1 and Supplementary Fig. S8d). This, however, does not mean that NIR increased in all pixels; rather it showed an average increase (i.e., the increase in NIR dominated the decrease in NIR in the region) (see Supplementary Fig. S9). Besides, compared with other vegetation types, the SW albedo anomaly increase was the strongest during OND droughts (0.005) (Table 1). In extreme wet events, however, the spectral changes showed a contrasting pattern in the VIS and NIR albedo as displayed in other vegetation types, with the magnitude of SW albedo decrease being stronger (−0.003) in both seasons (Table 1).

In grassland, the spectral changes in VIS and NIR albedo showed a similar contrasting pattern during extreme wet conditions in both seasons, but during MAM droughts it displayed a pattern similar to shrubland (i.e., both VIS and NIR albedo increased on average) (Fig. 3g and h). The SW albedo anomaly showed the biggest increase (0.005) during MAM droughts; this was due to a maximum increase in the VIS albedo anomaly (0.008) which was not counterbalanced by NIR albedo changes (0.001) (Table 1).

To understand the magnitude and statistical significance of albedo response to precipitation extremes, a quantile regression was applied (Fig. 4). With the exception of forests, the SW albedo anomaly had a statistically significant ($P < 0.01$) and negative relationship with SPI. Given the opposite spectral change between NIR and VIS albedo, forests showed the smallest change in SW albedo in all quantiles, followed by savanna. Furthermore, SW albedo anomalies were the least sensitive to drought and extreme wet events in forest and savanna, in both seasons, whereas shrubland showed the biggest SW albedo anomaly response to SPI changes in the region in all quantiles during OND, followed by grassland (Fig. 4b). During MAM, however, SW albedo anomaly responses to SPI change were stronger in grassland than in shrubland in all quantiles (Fig. 4a).

To examine the underlying process causing the spectral changes in albedo during precipitation extremes, the role of vegetation was inferred from the LAI anomaly (ΔLAI hereafter) (Fig. 5a and b) and the EVI anomaly (ΔEVI hereafter) (Fig. 5c and d). Both ΔLAI and ΔEVI consistently showed an opposite pattern to that of $\Delta\alpha_{VIS}$ and $\Delta\alpha_{SW}$ (except in forest) for both drought and extreme wet events (i.e., ΔLAI and ΔEVI decreased during drought and increased during extreme wet events across all vegetation types). With $\Delta\alpha_{NIR}$, ΔLAI and ΔEVI displayed a similar pattern in savanna, forest (except during extreme wet events in OND), and grassland (except during MAM drought). In shrubland, however, ΔLAI and ΔEVI exhibited an opposite pattern to that of $\Delta\alpha_{NIR}$ during drought events in both seasons.

3.2. Instantaneous shortwave surface radiative forcing due to albedo change during 2001–2016 precipitation extremes

The ISRF during precipitation extremes was computed using the SW broadband albedo shifts (Fig. 6). Forest and savanna, due to the strong opposing spectral changes between VIS and NIR albedo, exerted the smallest (near-zero) surface SW radiative forcing both during drought (-0.12 W m^{-2}, SD 0.03) and -0.38 W m^{-2}, SD 0.17) and extreme wet events (0.12 W m^{-2}, SD 0.14) and 0.14 W m^{-2}, SD 0.1) in OND, respectively (Fig. 6a and b). Unlike other vegetation types, forests showed inconsistencies in the radiative forcing sign between seasons (i.e., negative during MAM and positive during OND, in the extreme wet events).

Shrubland and grassland had relatively strong ISRF compared with forest and savanna The mean differences between shrubland/grassland and forest/savanna were also statistically significant ($P < 0.01$, unpaired t-test). During drought events, shrubland displayed an average ISRF ranging from -1 W m^{-2} (SD 0.27) in MAM to -1.28 W m^{-2} (SD 0.20) in OND, while grassland had an ISRF of -0.8 W m^{-2} (SD 0.17) in OND and -1.42 W m^{-2} (SD 0.49) in MAM on average (Fig. 6a). During extreme wet events (SPI > 1) shrubland had a slightly stronger radiative forcing of 0.71 W m^{-2} (SD 0.08) in OND and 0.72 W m^{-2} (SD 0.03) in MAM than grassland (0.45 W m$^{-2,}$ SD 0.12) in OND and 0.63 W m^{-2} (SD 0.07) in MAM in both seasons (Fig. 6b).

The regional ISRF was calculated from the sum of the average radiative forcing during drought (SPI ≤ 1) and extreme wet (SPI > 1) events from individual contributions of the four vegetation types (i.e., %forest × ISRF (forest) + %savanna × ISRF (savanna) + % shrubland × ISRF (shrubland) + %grassland × ISRF (grassland)). The results showed that during drought events, SW albedo increase exerted a regional ISRF of -0.64 W m^{-2} (SD 0.11) in MAM and -0.56 W m^{-2} (SD 0.16) in OND, whereas during extreme wet events, the regional ISRF was 0.33 W m^{-2} (SD 0.09) and 0.31 W m^{-2} (SD 0.09) for the corresponding seasons.

3.3. Impact on energy balance terms in the Horn of Africa

Anomalies of turbulent fluxes (latent and sensible heat fluxes) during 2001–2016 precipitation extremes are showed in Fig. 7a–d. With the exception of forest (during extreme wet periods), all vegetation
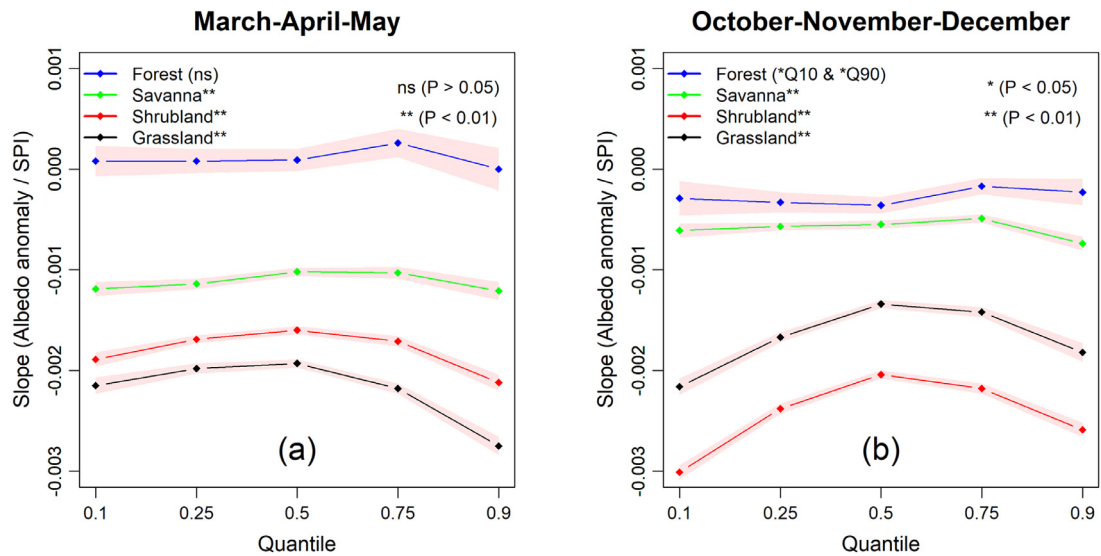
Fig. 4. Quantile regression slope for the 3-month Standardized Precipitation Index (SPI) (predictor variable) and shortwave broadband albedo anomaly (dependent variable) at 10th, 25th, 50th, 75th, and 90th percentile during 2001–2016 in the Horn of Africa across vegetation types in (a) March–May, (b) October–December . The shaded region shows the 95% confidence interval of the estimated regression coefficients (slopes).The ns refers to statistical non-significance ($P > 0.05$).

types consistently exhibited a negative latent energy anomaly (ΔLE) during drought and a positive ΔLE during extreme wet events, while the sensible heat flux displayed the opposite pattern in both drought and extreme wet events in all vegetation types. Furthermore, all anomalies had a significant relationship ($P < 0.01$) with precipitation extremes during both seasons, except in forest during OND (Supplementary Fig. S4).

Forest, compared with other vegetation types, displayed the smallest ΔLE decrease during OND drought (-2.69 W m^{-2}, SD 0.72). Furthermore, the extreme wet period changes in forest, in contrast to

the others, show a slight decrease in ΔLE (-1.64 W m^{-2}, SD 3.73 in OND), whereas grassland exhibited the biggest ΔLE changes during both drought and extreme wet events (i.e., grassland had a ΔLE of -28.10 W m^{-2} (SD 4.86) during OND drought and 24.51 W m^{-2} (SD 8.87) during MAM extreme wet periods). Savanna exhibited the second biggest ΔLE (-21.73 W m^{-2}, SD 5.37) in MAM during drought, followed by shrubland, while the extreme wet period ΔLE had a similar magnitude (~ 21 W m^{-2}) in savanna and shrubland.

The sensible heat flux anomaly (ΔH) showed an opposite change compared with ΔLE across vegetation types (i.e., it increased during
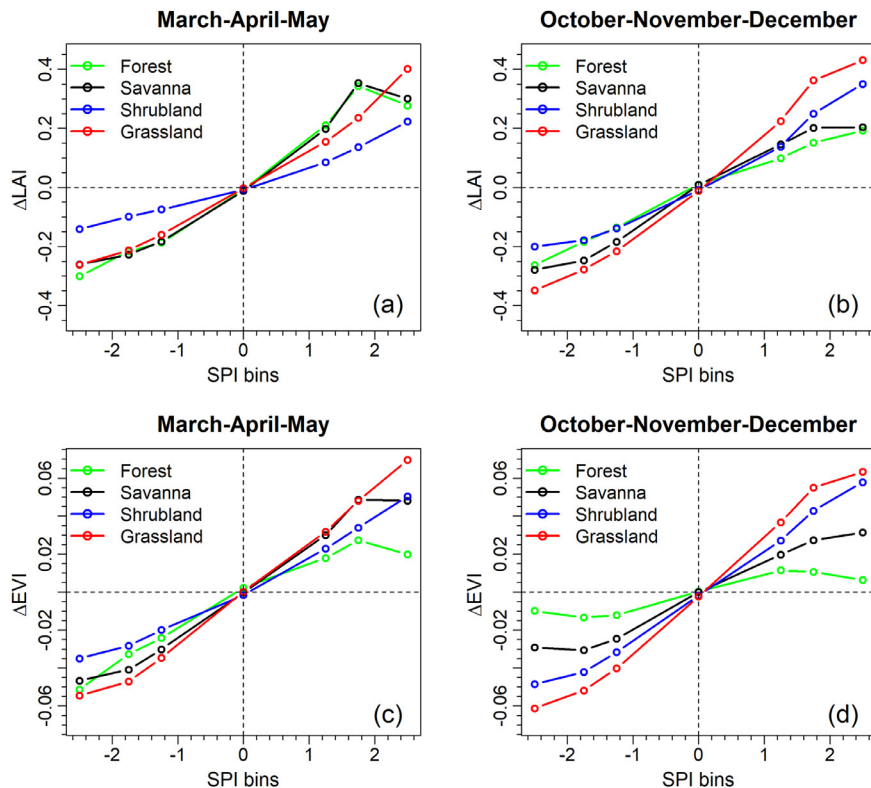
Fig. 5. Average leaf area index (LAI) and enhanced vegetation index (EVI) anomaly for each 3-month Standardized Precipitation Index (SPI) bin during March–April–May and October–November–December 2001–2016 in forest, savanna, shrubland, and grassland.
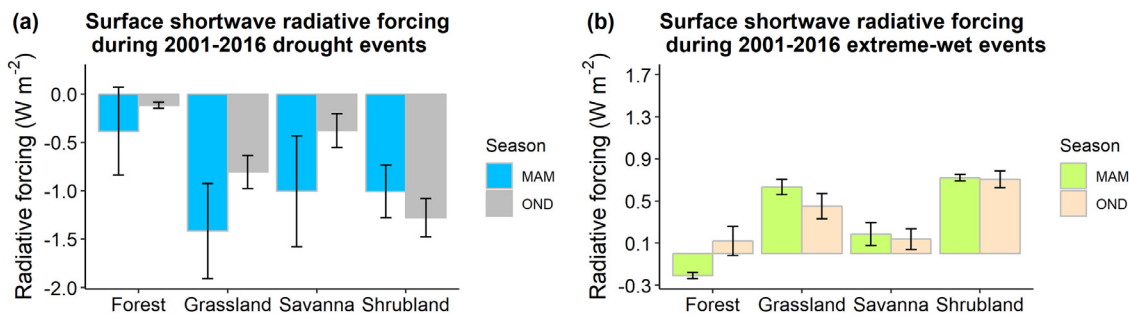
Fig. 6. Average instantaneous shortwave surface radiative forcing (ISRF) due to albedo changes during precipitation extremes in the four vegetation types (forest, savanna, shrubland, and grassland) in the Horn of Africa between 2001 and 2016. Panels a and b show ISRF during drought and extreme wet events, respectively. MAM , March, April, May ("long rains"); OND, October, November, December ("short rains"). Error bars show ± standard deviation.

drought and decreased during extreme wet events), except in forest (Fig. 7c and d). The magnitudes of ΔH were also comparable with ΔLE. Thus forest during OND drought had the smallest ΔH increase (1.42 W m^{-2}, SD 0.7) in OND, while grassland had the biggest ΔH in both drought (23.40 W m^{-2}, SD 4.13) in OND and extreme wet periods (−21.67 W m^{-2}, SD 7.91) in MAM. Similarly, savanna showed the second biggest ΔH increase (21.44 W m^{-2}, SD 5.02) in MAM followed by shrubland during drought, while the maximum extreme wet period ΔH was of similar magnitude (~ −19 W m^{-2}) in both savanna and shrubland.
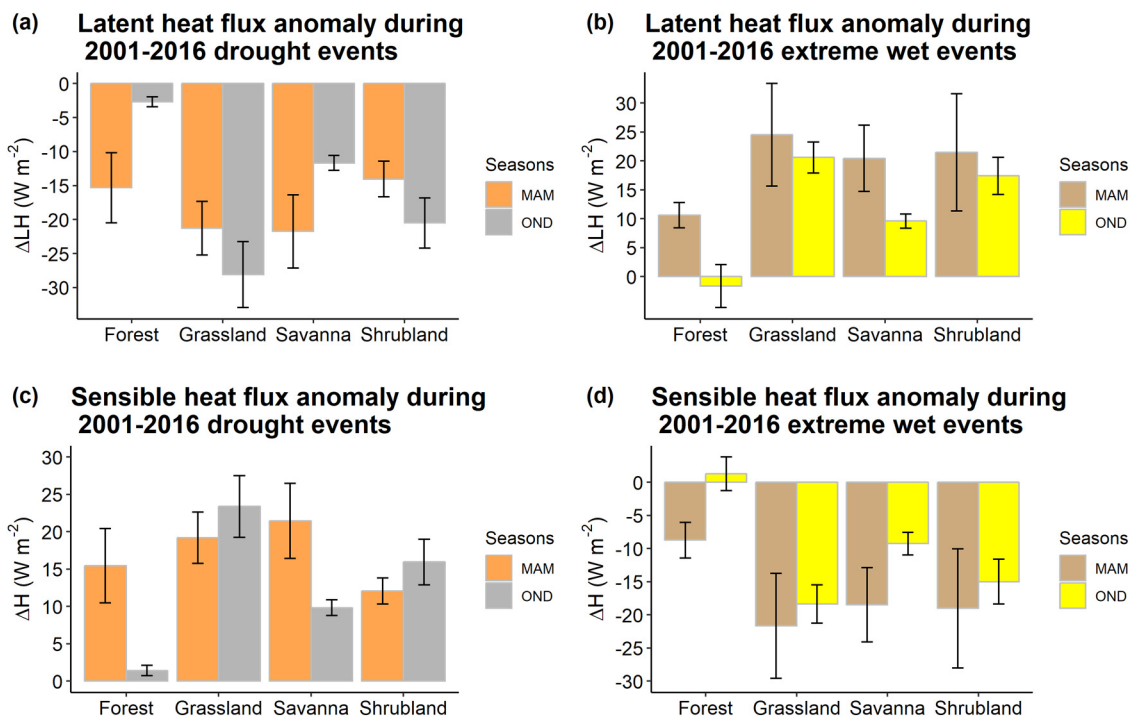
The radiation energy exchange anomalies during precipitation extremes are displayed in Fig. 8a–f. The incoming SW radiation anomaly (ΔSW_{in}) and the outgoing LW radiation anomaly (ΔLW_{out}) both increased during drought and decreased during extreme wet events, except for forest. In contrast, the net radiation anomaly (ΔR_n) exhibited the opposite pattern (i.e., decreased during drought and increased during extreme wet periods) (Fig. 8e and f). All anomalies displayed a significant relationship ($P < 0.05$) with precipitation extremes, except for forest ΔR_n during OND (Supplementary Fig. S5).

ΔSW_{in} was relatively bigger in savanna and forest during drought,

while it was the smallest for the same vegetation type during extreme wet periods. Forest, despite the stronger increase in ΔSW_{in} during drought, emitted the smallest ΔLW_{out} (3 W m^{-2}, SD 0.63) in OND and exhibited ~ 0 W m^{-2} ΔR_n in MAM during drought, whereas grassland emitted the strongest ΔLW_{out} (6.81 W m^{-2}, SD 1.07), closely followed by shrubland (6.27 W m^{-2}, SD 0.97). Hence, the strongest decrease in ΔR_n was in grassland (−4.70 W m^{-2}, SD 0.74) and shrubland (−4.55 W m^{-2}, SD 0.67). The extreme wet period ΔLW_{out} and ΔR_n were also dominated by the relatively stronger response from shrubland and grassland, whereas forest, followed by savanna, showed the smallest change (Fig. 8d and f).

3.4. Impact on the land surface temperature anomaly across vegetation types in the Horn of Africa

The mean temperature anomalies (ΔLST) during precipitation extremes (2001–2016) in forest, savanna, shrubland, and grassland are displayed in Fig. 9. All vegetation types consistently displayed an increase (decrease) in ΔLST during drought (extreme wet events). However, the magnitude of change varies between vegetation types. Forest

Fig. 7. Turbulent energy exchange anomalies (in W m^{-2}) during precipitation extremes in forest, grassland, savanna, and shrubland during 2001–2016. Panels a and b show latent heat flux anomalies, and c and d show sensible heat flux anomalies. Left and right panels display drought and extreme wet event changes, respectively. MAM, March, April, May ("long rains"); OND, October, November, December ("short rains"). Error bars show ± standard deviation.
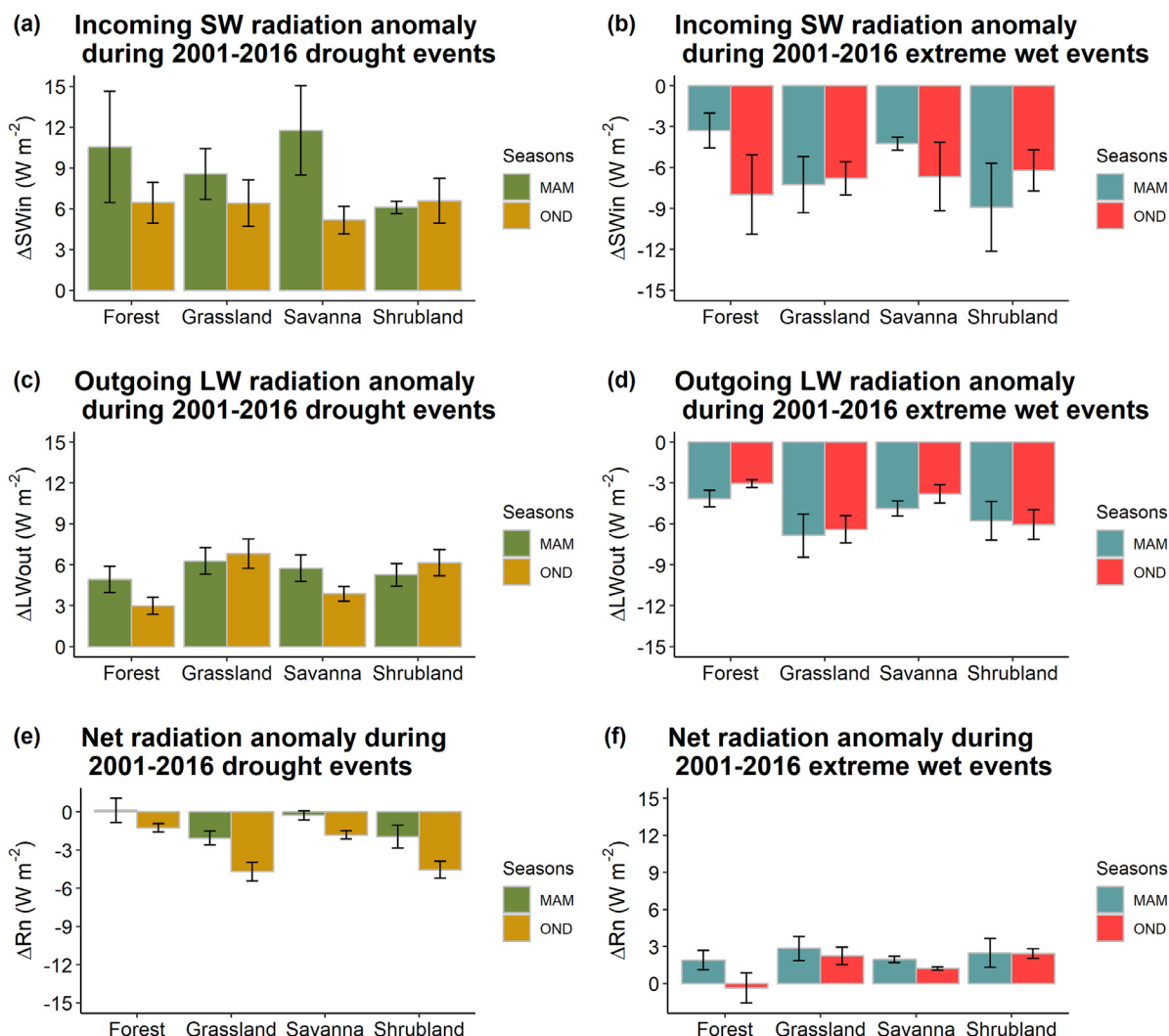
Fig. 8. Radiation energy exchange anomalies (in W m^{-2}) during 2001–2016 precipitation extremes in forest, grassland, savanna, and shrubland. Panels show incoming shortwave (SW) radiation (a and b), outgoing longwave (LW) radiation (c and d), and net radiation (e and f) anomalies. Left and right panels represent drought and extreme wet period changes, respectively. MAM, March, April, May ("long rains"); OND, October, November, December ("short rains"). Error bars show ± standard deviation.

and shrubland displayed the smallest average ΔLST of a similar magnitude (1.4 K) during drought in MAM. Besides, forest again showed the smallest ΔLST during extreme wet events in MAM (−0.95 K) and during both extreme wet (−0.74 K) and dry (0.63 K) events in OND, whereas the biggest ΔLST came from savanna (2.52 K in MAM and

1.37 K in OND) and grassland (1.74 K in MAM and 1.78 K in OND) during drought. During extreme wet events, however, the average ΔLST in grassland responded strongly (−2.33 K in MAM and −2.48 K in OND) and consistently in both seasons, followed by shrubland (−1.85 K and −2.04 K).
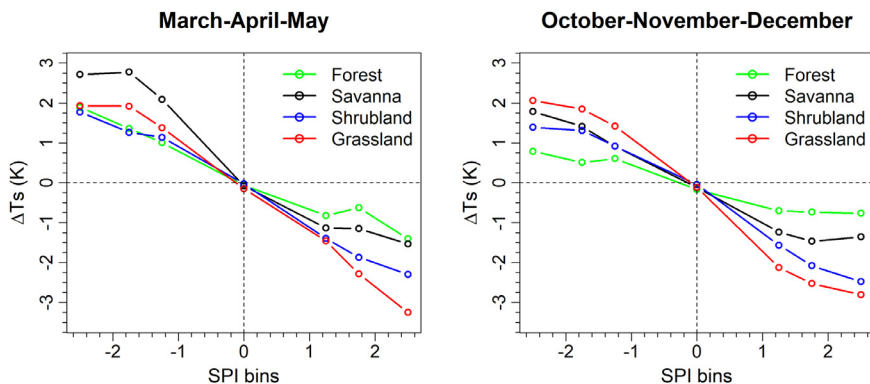
Fig. 9. Average land surface temperature anomaly for each 3-month Standardized Precipitation Index (SPI) bin during 2001–2016 precipitation extremes across forest, savanna, shrubland, and grassland in the Horn of Africa.
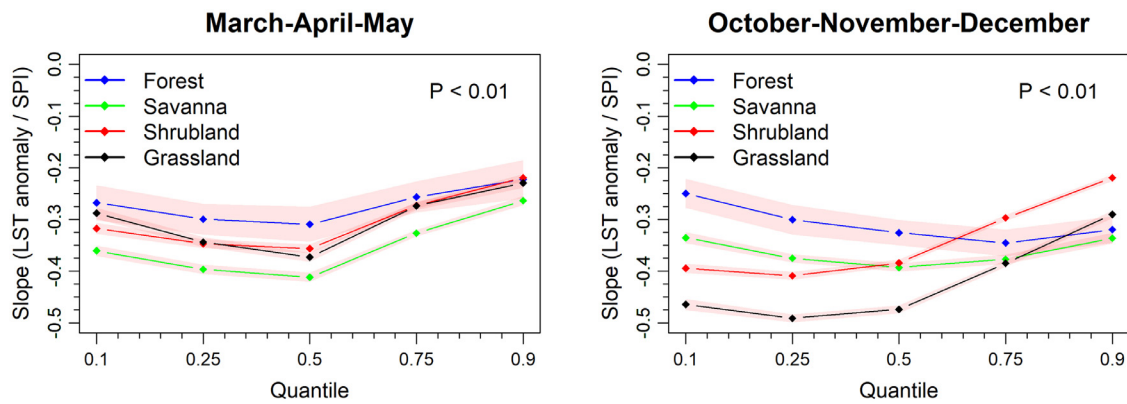
Fig. 10. Quantile regression slope for the 3-month Standardized Precipitation Index (SPI) (predictor variable) and land surface temperature (LST) anomaly (dependent variable) at 10th, 25th, 50th, 75th, and 90th percentile during 2001–2016 across vegetation types. Shaded region shows the 95% confidence interval of the estimated regression coefficients (slopes). All slopes were statistically significant ($P < 0.01$, two-tailed test).

The quantile regression results showed that the ΔLST response to both drought and extreme wet events was statistically significant ($P < 0.01$) in all vegetation types (forest, savanna, shrubland, and grassland) and precipitation extremes had an impact on LST anomalies in the region (Fig. 10). The impact was stronger in grassland (during OND) and savanna (MAM), while being weaker in forest in both seasons.

3.5. Difference between wet event and drought changes across vegetation types

As the difference between extreme wet and drought anomalies showed, the degree of sensitivity to precipitation extremes varied across vegetation types in the region (Table 2). Grassland, followed by shrubland, responded strongly to precipitation extremes, while forest displayed the smallest changes. Savanna exhibited the second smallest changes in precipitation extremes, except in LST.

4. Discussion

4.1. Changes in spectral albedo during precipitation extremes

Our results revealed that during 2001–2016 precipitation extremes, an increase in VIS albedo dominated during droughts, while a decrease was observed during extreme wet events. In forest and savanna, the opposing spectral changes in VIS and NIR albedo during drought largely averaged out, limiting the changes in SW albedo. Under severe drought conditions, as occurred during 2011, the VIS and NIR counterbalance can further limit the SW albedo changes in forest and savanna (Supplementary Fig. S6). Similar opposing changes in VIS and NIR albedo were reported in forest and woody savanna during the 2003 European heat wave and drought (Teuling and Seneviratne, 2008). Sütterlin et al. (2016) further showed that such opposing changes in albedo occur not only during drought but also during extreme wet and

normal precipitation events in Europe.

The mechanisms driving the observed spectral changes can be related to the soil-moisture depletion and the associated stress in vegetation (Lobell and Asner, 2002; Teuling and Seneviratne, 2008). Albedo is negatively related to soil-moisture content in all wavelengths (i.e., with a decrease in soil-moisture content, soil albedo increases and vice versa; however, the relationship is nonlinear and better described by exponential models) (Idso et al., 1975; Lobell and Asner, 2002). Hence during droughts, the decrease in soil moisture can contribute to an increase in VIS albedo. Besides, the consistent negative ΔLAI and ΔEVI during drought (Fig. 5) indicate vegetation stress and reduced chlorophyll production for photosynthesis, which might cause less absorption in the blue and red spectral regions (Gibson, 2000; Lillesand et al., 2008). Consequently, this leads to higher albedo in the blue and red spectral regions and an overall increase in the broadband VIS albedo anomaly. NIR albedo can decrease in stressed vegetation as NIR radiation can penetrate deep into the middle layer of the leaf's cell structure, where it will be absorbed by stressed mesophyll and palisade cells (Gibson, 2000). Moreover, the decrease in ΔLAI indicates a loss of leaves during drought and this can further contribute to the NIR albedo reduction.

Shrublands showed different NIR albedo patterns compared to the contrasting VIS and NIR patterns reported from previous studies in other vegetation class (e.g., Teuling and Seneviratne, 2008). Contrary to the expected reduction in NIR albedo associated with the decline in NIR reflectance from stressed vegetation (Fig. 5), the average NIR albedo increased in shrublands. This indicates that the NIR albedo changes in shrublands were not driven by vegetation changes, and can be explained by the background soil albedo changes. We observed that, in shrubland areas, the bare soil fraction (~60%) was dominantly higher than the vegetation cover fraction (~40%) (see Supplementary Fig. S10). During drought, the decrease in soil moisture can lead to an increase in bare soil reflectance in all wavelengths (Idso et al., 1975; Lobell and Asner, 2002). Consequently, the increase in NIR from bare

Table 2
Differences between 2001 and 2016 extreme wet and dry period anomalies of energy balance terms (R_n, net radiation; LH, latent heat flux; H, sensible heat flux; SW_{in}, incoming shortwave radiation; LW_{out}, outgoing longwave radiation), leaf area index (LAI), enhanced vegetation index (EVI), and land surface temperature (LST) during March–May and October–December. The range of values indicates variation between two seasons. IGBP, International Geosphere-Biosphere Programme.

Extreme wet – drought (Difference)

IGBP Vegetation type	ΔR_n (W m^{-2})	ΔLH (W m^{-2})	ΔH (W m^{-2})	ΔSW_{in} (W m^{-2})	ΔLW_{out} (W m^{-2})	ΔLAI	ΔEVI	ΔLST (K)
Forest	1–2	1–26	−0.1 to −24	−14	−6 to −9	0.3–0.5	0.02–0.06	−1 to −2
Savanna	2–3	21–42	−19 to −40	−12 to −16	−8 to −11	0.4–0.5	0.05–0.08	−3 to −4
Shrubland	4–7	35–38	−31	−13 to −15	−11 to −12	0.2–0.4	0.06–0.08	−3
Grassland	5–7	46–49	−41 to −42	−13 to −15	−13	0.5–0.6	0.09–0.1	−4

soil dominated the decrease in NIR albedo from stressed vegetation, resulting in a net increase in the average NIR albedo.

In grassland, unlike other vegetation types, variability in NIR albedo was shown to be seasonally dependent during drought. That is, different patterns were observed in MAM and OND. Contrary to previous studies that reported opposite VIS and NIR albedo changes during drought (Teuling and Seneviratne, 2008; Sütterlin et al., 2016), NIR albedo increased with VIS albedo during MAM. This seasonal variation can be related to the competing effects between soil and vegetation NIR albedo changes. The NIR albedo changes in soil and vegetation can vary with season as the fraction of bare soil and vegetation cover is not expected to be exactly the same in the two seasons. As the bare soil fraction from MOD44B indicated, grassland had a bare soil fraction of around 40% on average, under all precipitation conditions (normal, drought, and extreme wet) (Supplementary Fig. S10). Hence during drought, with an increase in vegetation stress, more soils will be exposed to the surface and the proportion of bare soil fraction can increase, and thus the NIR albedo can increase/decrease depending on the dominant effect between soil and vegetation in the two seasons. This result indicates that the average NIR albedo change in grassland can vary depending on the season, bare soil fraction, and geographical location during drought, which was not yet reported in previous studies (e.g., Teuling and Seneviratne, 2008). However, further investigation using ground albedo data are needed to accurately quantify the impact of soil and vegetation fraction change on the seasonal variation of NIR albedo in grassland, where the proportions of vegetation and the soil fraction can increase to comparable magnitude.

Changes in albedo during extreme wet events were rather consistent and opposite to that of the drought season changes in all vegetation types, except forests. In forests, the ΔSW albedo anomaly increased, driven by the stronger increase in NIR that outweighed the decrease in the VIS albedo anomaly during MAM. We argue that this pattern is explained by the enhanced greening during MAM compared with the negligible changes during OND (i.e., spectral changes during this season were negligible in all parts of the spectrum) (Fig. 3b). With the enhanced soil-moisture condition in the extreme wet periods, vegetation productivity increases (Fig. 5) and photosynthetic activity will be enhanced. This will cause more absorption of blue and red radiation for photosynthesis and more scattering of NIR radiation from green leaves, which can lead to a decrease in VIS albedo and an increase in NIR albedo. Soil reflectance in contrast decreases in all wavelengths during extreme wet periods and can contribute to a reduction in albedo (Gibson, 2000; Lillesand et al., 2008).

The magnitude of SW albedo changes during droughts was larger than during extreme wet events. This can be partly related to the saturation of soil reflectance at lower soil-moisture content (i.e., around 20% volumetric water content) (Lobell and Asner, 2002), which can contribute to the smaller changes in the resulting SW albedo. Furthermore, unlike extreme wet periods, VIS albedo anomalies during droughts increased consistently and linearly for each step increase in drought severity level (except in forests) (Fig. 3). This further indicates that albedo is more likely to be affected by droughts than extreme wet events.

4.2. Energy exchange during precipitation extremes and its impact on climate

The ISRF was relatively strong in shrubland and grassland, compared with forest and savanna, due to their relatively larger SW albedo changes during precipitation extremes. Furthermore, as much of the study area (around 50%) was covered by shrubland and grassland, their contributions to regional surface radiative forcing were also relatively high (i.e., 80–93% and 92–95% of the regional ISRF during drought and extreme wet periods, respectively). The magnitude of the regional ISRF associated with extreme wet periods (0.31 to 0.33 W m^{-2}) was smaller than during droughts (-0.56 to -0.64 W m^{-2}). Hence, in all extreme

events, SW albedo changes had a small impact on the regional net SW radiation.

Although the impact of albedo change on ISRF can be locally as high as -8 W m^{-2} in some pixels during strong drought events (e.g., during the 2011 Horn of Africa drought; Supplementary Fig. S7), its regional impact on average was too small (-0.56 to -0.64 W m^{-2}) to affect surface-atmosphere link during 2001–2016. Other studies in Europe also reported smaller magnitude (–1 W m^{-2}) at regional scale during drought (e.g., Teuling and Seneviratne, 2008). Our results support previous findings in forests and savanna showing that albedo changes during extreme events had limited impact on the coupling between the land surface and atmosphere (Teuling and Seneviratne, 2008). Hence, as albedo changes affected the available net SW radiation by only a small fraction (< 3%), the remaining energy was channeled to turbulent energy fluxes.

Our results showed that energy fluxes and LST had opposite patterns when drought and extreme wet events were compared. During drought, anomalies of incoming SW radiation increased, latent heat flux decreased, sensible heat flux increased, and LST increased. The reverse pattern occurred during extreme wet events. The significant ($P < 0.01$) increase (decrease) in the SW radiation anomaly can be explained by the decrease (increase) in cloud cover and water vapor in the atmosphere during drought (extreme wet periods) (Greene et al., 2011). With decreased cloud cover during drought, more radiation load is expected and the reverse would occur during extreme wet events. In semi-arid, water-limited environments, the increase in LST is likely due to the reduction in evaporative cooling associated with less evapotranspiration following soil-moisture stress. The opposite would occur during extreme wet periods. These explanations are supported by both ground and satellite observations (Whelan et al., 2015; Yin et al., 2014; Alexander, 2011; Jung et al., 2010; Meyers 2001).

Furthermore, the decline in net radiation during drought and the increase during extreme wet periods across vegetation types, except in forests, can be related to the changes in albedo, surface temperature, and upwelling LW radiation (Eltahir, 1998). This means that in addition to the reduction in net radiation during drought caused by the albedo effect, a reduction in evapotranspiration raises the LST, which in turn increases the emitted LW radiation and hence decreases net radiation (Fig. 8) (Yin et al., 2014; Small and Kurc, 2003).

Although forest areas were exposed to a stronger incoming SW radiation anomaly, they responded the least to precipitation extremes, as indicated by the smallest anomalies in turbulent and radiation energy exchange, LST, as well as minor changes in vegetation conditions (Table 2). The small decrease in latent heat flux during drought indicates that the impact of drought in limiting evapotranspiration was relatively small and some of the extra energy is likely used for evapotranspiration. Forests can access groundwater through their deep rooting system and are able to regulate water loss through stomatal closure, being able to endure mild drought conditions (Kerhoulas et al., 2013; Ehleringer and Dawson, 1992; Kramer and Boyer, 1995). But with prolonged and severe drought, followed by increasing temperature and aridity, forests become vulnerable to hydraulic failure, and subsequent tree mortality can occur (Choat et al., 2012; Allen et al., 2010; Williams et al., 2012).

Savanna exhibited the second smallest anomalies in response to rainfall extremes, except in LST. The LST anomaly difference between extreme wet and drought in savanna ranges from -3 K to the highest in the region (-4 K). This characteristic can be explained by the stronger latent and sensible heat flux anomaly ranges of savanna, which had comparable magnitude to those of grassland (Table 2). The rationale behind the range of LST anomalies (-3 to -4 K) in savanna is likely related to its plant composition. As a mix of trees and grasses coexist in savanna, they can compete or support each other during precipitation extremes (Dohn et al., 2013). The occurrence of trees in savanna might counteract, to a smaller degree, the impact of drought by limiting the reduction in latent heat flux and increasing resilience to drought

(Whelan et al., 2015). Furthermore, in such a water-limited environment, trees can help to reduce water stress in grasses by lifting water from groundwater to the top dry soil layer via their roots and minimizing incoming SW radiation (Dohn et al., 2013).

In contrast, grassland responded strongly to precipitation extremes. It showed the strongest anomalies in all variables, except in incoming SW anomalies (Table 2). Previous studies also showed strong sensitivity of grassland to water availability in semi-arid environments (Huxman et al., 2004; Knapp and Smith, 2001). Grassland, due to its shallow rooting systems, responds quickly to water stress but also recovers fast when soil-moisture conditions improve. This characteristic likely caused the changes observed in grassland during precipitation extremes. Furthermore, the strong net radiation and turbulent flux anomalies in grassland and shrubland might indicate greater influence of soil-moisture variability in a semi-arid environment (Jung et al., 2010; Small and Kurc, 2003). Besides, compared with other vegetation types, the stronger reduction in evaporative cooling and concurrent increase in sensible heat flux anomaly during drought, with larger magnitude, might be explained by the use of much of the incoming radiation to strongly increase the LST anomalies, which in turn caused strong upwelling LW irradiance in grassland (Fig. 8). Our results are in line with previous studies during the 2003 European heat wave and drought (Teuling et al., 2010), in which a stronger heating from grassland compared with forest was reported under longer timescale conditions.

Shrubland displayed the second strongest anomalies in most variables. Given the arid characteristics of this vegetation type, a stronger influence of soil-moisture variability is expected (Jung et al., 2010), whereas the smaller changes in vegetation status (ΔLAI and ΔEVI) during droughts, in comparison with grassland, imply stronger resilience to water shortage (Varela et al., 2016). Shrubland can survive longer during water stress by maintaining turgor through osmotic adjustment and changing cellular elasticity and oxidant mechanisms (Reddy et al., 2004). Associated with the smaller vegetation stress condition, a relatively low reduction in latent heat flux and surface temperature anomaly can thus be expected in shrubland (Table 2).

It is interesting that grassland and shrubland, despite having bigger and positive shortwave radiative forcing, exhibited the strongest net surface warming during OND drought. This shows that the surface cooling from the strong shortwave albedo feedback was outweighed by the warming from the reduction in latent heat flux and resulting in higher sensible heat flux and land surface temperature. Given strong surface feedback from moisture recycling in the region (Notaro et al., 2019), this process can reduce moisture and increase heat at the atmospheric boundary layer, limiting cloud formation (Miralles et al., 2018) and, consequently, amplifying surface warming and intensifying drought events. For more information on surface feedbacks, refer the conceptual flow diagram in the supplementary material (Fig. S11).

5. Conclusions

In this paper, we analyzed the impact of precipitation extremes on albedo, energy exchange, and surface temperature anomalies across four vegetation types (shrubland, grassland, savanna, and forest) in the Horn of Africa. The VIS albedo showed a stronger response to precipitation extremes compared with NIR albedo. Opposite changes in VIS and NIR albedo generally canceled each other in forest and savanna, limiting albedo changes when considering the entire SW spectrum. This pattern was not observed in shrubland and grassland, where both VIS and NIR albedo increased during droughts, contributing for a stronger shortwave radiative forcing. We demonstrated that the increase in NIR albedo in shrubland and grassland was caused by the dominant influence of bare soil NIR albedo, which was weakly counterbalanced by vegetation NIR albedo decrease.

At a regional level, the ISRF due to albedo change was small both during drought (-0.56 to $-0.64\,\mathrm{W\,m^{-2}}$) and extreme wet events (0.31

to $0.33\,\mathrm{W\,m^{-2}}$). Hence our results support the view that drought-induced changes in albedo are not strong enough to influence the surface–atmosphere coupling. In contrast, precipitation extremes had a stronger impact on the exchange of latent and sensible heat, leading to a surface feedback that contributed to LST anomalies during these extreme events, except in forests. When the impact of precipitation extremes on the radiation balance and turbulent fluxes was compared across vegetation types, grassland was found to be the most sensitive, while forest was relatively resilient. These results highlight the attractiveness of forest preservation and afforestation to counteract the climatic impact of drought through regulating net radiation and LST anomalies.

References

Abera, T.A., Heiskanen, J., Pellikka, P.K.E., Maeda, E.E., 2018. Rainfall-vegetation interaction regulates temperature anomalies during drought events in the horn of Africa. Glob. Planet. Change 167, 35–45. https://doi.org/10.1016/j.gloplacha.2018.05.002.

Abera, T.A., Heiskanen, J., Pellikka, P.K.E., Rautiainen, M., Maeda, E.E., 2019. Clarifying the role of radiative mechanisms in the spatio-temporal changes of land surface temperature across the Horn of Africa. Remote. Sens. Environ 221, 210–224. https://doi.org/10.1016/j.rse.2018.11.024.

Alexander, L., 2011. Extreme heat rooted in dry soils. Nat. Geosci. 4, 12–13. https://doi.org/10.1038/ngeo1045.

Allen, C.D., et al., 2010. Global overview of drought and heat-induced tree mortality reveals emerging climate change risks for forests. For. Ecol. Manag. 259, 660–684. https://doi.org/10.1016/j.foreco.2009.09.001.

Bastiaanssen, W.G.M., 2000. SEBAL-based sensible and latent heat fluxes in the irrigated Gediz Basin, Turkey. J. Hydrol. 229, 87–100. https://doi.org/10.1016/S0022-1694(99)00202-4.

Betts, A.K., Ball, J.H., 1998. FIFE surface climate and site-average dataset 1987–89. J. Atmos. Sci. 55, 1091–1108.

Charney, J., Stone, P.H., Quirk, W.J., 1975. Drought in the Sahara: a biogeophysical feedback mechanism. Science 187, 434–435.

Choat, B., et al., 2012. Global convergence in the vulnerability of forests to drought. Nature 491, 752–755.

Dimiceli, C., Carroll, M., Sohlberg, R., Kim, D.H., Kelly, M., Townshend, J.R.G., 2015. MOD44B MODIS/Terra Vegetation Continuous Fields Yearly L3 Global 250 m SIN Grid V006. NASA EOSDIS Land Processes DAAChttps://doi.org/10.5067/MODIS/MOD44B.006.

Dingman, S.L., 2015. Physical Hydrology, 3rd ed. Waveland Press, Long Grove, IL.

Dohn, J., et al., 2013. Tree effects on grass growth in savannas: competition, facilitation and the stress-gradient hypothesis. J. Ecol. 101, 202–209. https://doi.org/10.1111/1365-2745.12010.

Dong, X., Minnis, P., Xi, B., Sun-Mack, S., Chen, Y., 2008. Comparison of CERES-MODIS stratus cloud properties with ground-based measurements at the DOE ARM Southern great plains site. J. Geophys. Res.-Atmos. 113, D03204. https://doi.org/10.1029/2007JD008438.

Ehleringer, J.R., Dawson, T.E., 1992. Water uptake by plants: perspectives from stable isotope composition, 1073–1082. Plant Cell Environ. 15, 1073–1082. https://doi.org/10.1111/j.1365-3040.1992.tb01657.x.

Eltahir, E.A.B., 1998. A soil moisture rainfall feedback mechanism: 1. theory and observations. Water Resour. Res. 34, 765–776.

Evans, J.P., Meng, X., Mccabe, M.F., 2017. Land surface albedo and vegetation feedbacks

enhanced the millennium drought in south-east Australia. Hydrol. Earth Syst. Sci. 21, 409–422. https://doi.org/10.5194/hess-21-409-2017.

Friedl, M., Sulla-Menashe, D., 2015. MCD12Q1 MODIS/Terra + Aqua Land Cover Type Yearly L3 Global 500 m SIN Grid V006. NASA EOSDIS Land Processes DAAChttps://doi.org/10.5067/MODIS/MCD12Q1.006.

Gao, M., Franzke, C.L.E., 2017. Quantile regression–based spatiotemporal analysis of extreme temperature change in China. Int. J. Climatol. 30, 9897–9900. https://doi.org/10.1175/JCLI-D-17-0356.1.

Gibson, P.J., 2000. Introductory Remote Sensing: Principles and Concepts. Routledge, London.

Greene, H., Leighton, H.G., Stewart, R.E., 2011. Drought and associated cloud fields over the Canadian prairie provinces drought and associated cloud fields over the Canadian Prairie Provinces. Atmos Ocean. 49, 356–365. https://doi.org/10.1080/07055900.2011.559771.

Huete, A., Didan, K., Miura, T., Rodriguez, E.P., Gao, X., Ferreira, L.G., 2002. Overview of the radiometric and biophysical performance of the MODIS vegetation indices. Remote. Sens. Environ. 83, 195–213. https://doi.org/10.1016/S0034-4257(02)00096-2.

Huffman, J.G., Adler, R.F., Bolvin, D.T., Nelkin, E.J., 2010. The TRMM multi-satellite precipitation analysis (TMPA). Satellite Rainfall Applications For Surface Hydrology. Springer, Dordrecht, pp. 3–22. https://doi.org/10.1007/978-90-481-2915-7.

Huxman, T.E., et al., 2004. Convergence across vegetation types to a common rain-use efficiency. Nature 429, 651–654.

Idso, S.B., Jackson, R.D., Reginato, R.J., Kimball, B.A., Nakayama, F.S., 1975. The dependence of bare soil albedo on soil water content. J. Appl. Meteorol. 14, 109–113.

Indeje, M., Semazzi, F.H.M., Ogallo, L.J., 2000. ENSO signals in East African rainfall seasons. Int. J. Climatol. 20, 19–46. https://doi.org/10.1002/(SICI)1097-0088(200001)20:1<19::AID-JOC449>3.0.CO;2-0.

Jung, M., Reichstein, M., Ciais, P., Seneviratne, S.I., Sheffield, J., Goulden, M.L., ... Zhang, K., 2010. Recent decline in the global land evapotranspiration trend due to limited moisture supply. Nature 467, 951–954.

Kerhoulas, L.P., Kolb, T.E., Hurteau, M.D., Koch, G.W., 2013. Managing climate change adaptation in forests: a case study from the U.S. Southwest. J. Appl. Ecol. 50, 1311–1320. https://doi.org/10.1111/1365-2664.12139.

Knapp, k.A., Smith, M.d., 2001. Variation among vegetation types in temporal dynamics of aboveground primary production. Science 291, 481–484. https://doi.org/10.1126/science.291.5503.481.

Koenker, R., 2005. Quantile Regression. Cambridge University Press ISBN 0-521-60827-9.

Kramer, P.J., Boyer, J.S., 1995. Water Relations of Plants and Soils. Academic Press, Inc.

Li, C., Chai, Y., Yang, L., Li, H., 2016. Spatio-temporal distribution of flood disasters and analysis of influencing factors in Africa. Nat. Hazards 82, 721–731. https://doi.org/10.1007/s11069-016-2181-8.

Li, Z., Tang, H., Zhang, B., Yang, G., Xin, X., 2015. Evaluation and intercomparison of MODIS and GEOV1 global leaf area index products over four sites in North China. Sensors 15, 6196–6216. https://doi.org/10.3390/s150306196.

Liang, S., 2001. Narrowband to broadband conversions of land surface albedo I: algorithms. Remote. Sens. Environ. 76, 213–238. https://doi.org/10.1016/S0034-4257(00)00205-4.

Liang, S., Liu, Q., 2012. Global Land Surface Products, Albedo Product Data Collection (1985–2010). Beijing Normal Universityhttps://doi.org/10.6050/glass863.3001.db.

Lillesand, T.M., Kiefer, R.W., Chipman, J.W., 2008. Remote Sensing and Image Interpretation, 6th Edn. John Wiley & Sons, Hoboken.

Lobell, D.B., Asner, G.P., 2002. Moisture effects on soil reflectance. Soil Sci. Soc. Am. J. 66, 722–727.

Loeb, N.G., Wielicki, B.A., Doelling, D.R., Smith, G.L., Keyes, D.F., Kato, S., Wong, T., 2009. Toward optimal closure of the earth's top-of-atmosphere radiation budget. J. Clim. 22, 748–766. https://doi.org/10.1175/2008JCLI2637.1.

Luyssaert, S., et al., 2014. Land management and land-cover change have impacts of similar magnitude on surface temperature. Nat. Clim. Change 4, 389–393.

Lyon, B., DeWitt, D.G., 2012. A recent and abrupt decline in the East African long rains. Geophys. Res. Lett. 39, L02702. https://doi.org/10.1029/2011GL050337.

Martens, B., Miralles, D.G., Lievens, H., van der Schalie, R., de Jeu, R.A.M., Fernández-Prieto, D., Beck, H.E., Dorigo, W.A., Verhoest, N.E.C., 2017. GLEAM v3: satellite-based land evaporation and root-zone soil moisture. Geosci. Model Dev. 10, 1903–1925.

Masih, I., Maskey, S., Mussá, F.E.F., Trambauer, P., 2014. A review of droughts on the African continent: a geospatial and long-term perspective. Hydrol. Earth Syst. Sci. 18, 3635–3649. https://doi.org/10.5194/hess-18-3635-2014.

Meng, X.H., Evans, J.P., McCabe, M.F., 2014a. The impact of observed vegetation changes on land–atmosphere feedbacks during drought. J. Hydrometeorol. 15, 759–776. https://doi.org/10.1175/JHM-D-13-0130.1.

Meng, X.H., Evans, J.P., McCabe, M.F., 2014b. The influence of inter-annually varying albedo on regional climate and drought. Clim. Dynam. 42, 787–803. https://doi.org/10.1007/s00382-013-1790-0.

Meyers, T.P., 2001. A comparison of summertime water and CO_2 fluxes over rangeland for well watered and drought conditions. Agric. For. Meteorol. 106 (3), 205–214.

Michael, G.B., et al., 2015. Technical Report Series on Global Modeling and Data Assimilation, 43. . https://gmao.gsfc.nasa.gov/pubs/docs/Vernieres589.pdf, Accessed date: 2 May 2018.

Miralles, D.G., Gentine, P., Seneviratne, S.I., Teuling, A.J., 2018. Land-atmospheric feedbacks during droughts and heatwaves: state of the science and current challenges. Ann. N. Y. Acad. Sci. https://doi.org/10.1111/nyas.13912. Special Issue: Climate Sciences. ISSN 0077-8923.

NASA LP DAAC, 2014. MCD43B1 BRDF-Albedo Model Parameters 8-Day L3 Global 1 km, Version 5, NASA EOSDIS Land Processes DAAC. USGS Earth Resources Observation and Science (EROS) Center, Sioux Falls, South Dakota. https://lpdaac.usgs.gov, Accessed date: 10 December 2016.

Naumann, G., Barbosa, P., Carrao, H., Singleton, A., Vogt, J., 2012. Monitoring drought conditions and their uncertainties in Africa using TRMM data. J. Appl. Meteorol. Climatol. 51, 1867–1874. https://doi.org/10.1175/JAMC-D-12-0113.1.

Nicholson, S.E., 2017. Climate and climatic variability of rainfall over eastern Africa. Rev. Geophys. 55, 590–635. https://doi.org/10.1002/2016RG000544.

Notaro, M., Wang, F., Yu, Y., 2019. Elucidating observed land surface feedbacks across sub-Saharan Africa. Clim. Dyn. 1–23. https://doi.org/10.1007/s00382-019-04730-3.

Reddy, A.R., Chaitanyaa, K.V., Vivekanandan, M., 2004. Drought-induced responses of photosynthesis and antioxidant metabolism in higher plants. J. Plant Physiol. 161, 1189–1202.

Schaaf, C., Wang, Z.: MCD43C3 MODIS/Terra + Aqua BRDF/Albedo Albedo Daily L3 global 0.05Deg CMG V006, NASA EOSDIS Land Processes DAAC, doi: 10.5067/MODIS/MCD43C3.006, 2015.

Small, E.E., Kurc, S.A., 2003. Tight coupling between soil moisture and the surface radiation budget in semiarid environments: implications for land-atmosphere interactions. Water Resour. Res. 39, 1278. https://doi.org/10.1029/2002WR001297.

Sütterlin, M., Stöckli, R., Schaaf, C.B., Wunderle, S., 2016. Albedo climatology for European land surfaces retrieved from AVHRR data (1990–2014) and its spatial and temporal analysis from green-up to vegetation senescence. J. Geophys. Res. Atmos. 121, 8156–8171. https://doi.org/10.1002/2016JD024933.

Teuling, A.J., Seneviratne, S.I., 2008. Contrasting spectral changes limit albedo impact on land-atmosphere coupling during the 2003 European heat wave. Geophys. Res. Lett. 35, L03401. https://doi.org/10.1029/2007GL032778.

Teuling, A.J., et al., 2010. Contrasting response of European forest and grassland energy exchange to heatwaves. Nat. Geosci. 3 (10), 722–727. https://doi.org/10.1038/ngeo950.

Tropical Rainfall Measuring Mission (TRMM), 2011. TRMM (TMPA/3B43) Rainfall Estimate L3 1 Month 0.25 Degree x 0.25 Degree V7. Goddard Earth Sciences Data and Information Services Center, Greenbelt, MD. https://doi.org/10.5067/TRMM/TMPA/MONTH/7. GES DISC.

UNDP (United Nations Development Programme): Crisis brief: Horn of Africa, One United Nations Plaza New York, NY, 10017 USA, http://www.undp.org/content/dam/undp/library/crisis%20prevention/UNDP%20Crisis_brief_horn_of_africa.pdf, 2011.

Varela, M.C., Arslan, I., Reginato, M.A., Cenzano, A.M., Luna, M.V., 2016. Phenolic compounds as indicators of drought resistance in shrubs from Patagonian shrublands (Argentina). Plant Physiol Biochem. 104, 81–91. https://doi.org/10.1016/j.plaphy.2016.03.014.

Verger, A., Camacho, F., Goten, R.V., Jacobs, T.: Product user manual, Leaf area index (LAI), fraction of absorbed photosynthetically active radiation (FAPAR), fraction of vegetation cover (FCover), collection 1 km, version 2. Issue 1.32. Copernicus, 2014.

Wan, Z., Hook, S., Hulley, G., 2015. MOD11A2 MODIS/Terra Land Surface Temperature/Emissivity 8-Day L3 Global 1 km SIN Grid V006. NASA EOSDIS LP DAAChttps://doi.org/10.5067/modis/mod11a2.006.

Whelan, A., Starr, G., Staudhammer, C.L., Loescher, H.W., Mitchell, R.J., 2015. Effects of drought and prescribed fire on energy exchange in longleaf pine ecosystems. Ecosphere 6, 128. https://doi.org/10.1890/ES15-00111.1.

Williams, A.P., et al., 2012. Drought stress and tree mortality. Nat. Clim. Change 3, 292–297. https://doi.org/10.1038/nclimate1693.

WMO (World Meteorological Organization), 2012. Standardized Precipitation Index User Guide. In: Svoboda, M., Hayes, M., Wood, D. (Eds.), Standardized Precipitation Index User Guide. WMO, Geneva -No. 1090.

Yin, D., Roderick, M.L., Leech, G., Sun, F., Huang, Y., 2014. The contribution of reduction in evaporative cooling to higher surface air temperatures during drought. Geophys.Res.Lett. 41, 7891–7897. https://doi.org/10.1002/2014GL062039.

Zhang, X., Friedl, M.A., Schaaf, C.B., Strahler, A.H., Liu, Z., 2005. Monitoring the response of vegetation phenology to precipitation in Africa by coupling MODIS and TRMM instruments. J. Geophys. Res. Atmos 110, 1–14. https://doi.org/10.1029/2004JD005263.